

Chapter

Low-Frequency Bandgaps by Topological Acoustic Black Holes

Jie Deng

Abstract

Nowadays, acoustic black holes (ABHs) are very popular for producing efficient vibration reduction at high frequencies in combination with some damping mechanisms. However, its low-frequency performance is hard to improve since the ABH effect principally occurs beyond its cut-on frequency. Fortunately, periodic ABH configuration offers some bandgaps below that frequency for wave attenuation. In this chapter, a topological ABH structure is suggested to produce a new bandgap at very low frequencies, by taking a supercell and decreasing the ABH distance. The wave and Rayleigh-Ritz method (WRRM) is adopted to compute the complex dispersion curves. Examinations of the dispersion curves and transmissibilities confirm the efficiency of the low-frequency vibration reduction capability of the proposed topological ABHs.

Keywords: acoustic black holes, topological bandgaps, low frequencies, vibration reduction, complex dispersion curves

1. Introduction

Acoustic black holes (ABHs) in mechanics are very efficient for wave manipulation in structures. By decreasing structural thickness following a power law, the impinging wave can be significantly retarded and concentrated as it propagates to the tip. Usually, in the vicinity of the ABH tip, some damping mechanisms [1, 2] are adopted; thus, the vibration energy is converted to, for example, heat, resulting in highly efficient vibration attenuation. However, there exists a cut-on frequency that relies on the ABH size. It is generally thought that the ABH effect can only be efficient above that frequency. While in practical engineering situations the tough task is related to low frequencies. Therefore, it is imperative to ameliorate the low-frequency performance of ABH structures.

Periodic distribution of ABHs [3–5], a new type of phononic crystal/metamaterial, could produce some bandgaps below the cut-on frequency, constituting a promising approach for low-frequency vibration reduction. This concept is first investigated in Refs. [6–8], where the purpose is to modulate the wavefront of bending waves in plates. Later, a periodic ABH beam is proposed [9], reporting that many locally resonant low-frequency bandgaps are formed below the cut-on frequency. Recently, it has been unveiled that these bandgaps are caused by Bragg scattering [10].

Interestingly, a compound ABH beam structure (also called double-leaf ABH beam) has been extensively studied [11–13], due to that many broad bandgaps can be found. In Ref. [14], very low bangaps are obtained by modifying the ABH parameters. Nevertheless, it is very tricky to obtain complete bandgaps in plates. In Ref. [15], a circular double-leaf ABH structure is proposed, showing that complete and sub-wavelength bandgaps are found. While in Ref. [16], a strip ABH is proposed, providing broad bandgaps and showing promising application for wave manipulation in plates. On the other hand, periodically placing resonators on the ABH plate has also been investigated [17, 18], where a very low bandgap is formed to suppress the first formant of the plate. Not only that, nonlinear effect has been applied for ABHs, taking the advantage of energy transfer from low to high frequencies [19]. Recently, as an alternative of embedded ABHs, the additive ABHs have been widely explored, showing that the added mass could somehow facilitate low-frequency wave reduction [20–23].

To further improve the low-frequency performance of embedded ABHs, we must resort to the combination of different physics. Inspired by topological metamaterials, in the current chapter, we propose topological ABHs to generalize a low-frequency bandgap, by adjusting the ABH distance in a supercell, as illustrated in **Figure 1**. It is worthwhile mentioning that the concept of topology has been introduced in previous works [24, 25]. However, the purpose of those works is concentrated on the presence of robust edge or surface states within the bandgap. Very differently, in the current chapter, we exploit the low-frequency bandgap generalized by the topological ABHs, to further enhance the low-frequency performance of ABHs. Please note that it is easy to prove the topological property by showing, for example, interface states or topological symmetry. We will overlook that because the focus is only placed on generating low-frequency bandgaps.

To unveil the properties of the proposed topological ABHs, we adopt our previously established wave and Rayleigh-Ritz method (WRRM, see [18, 26]) to recover the complex dispersion curves, where the imaginary part stands for the wave attenuation (including damping and bandgaps). Furthermore, the transmissibilities of finite structures will also be tested, to prove the existence of low-frequency topological bandgap.

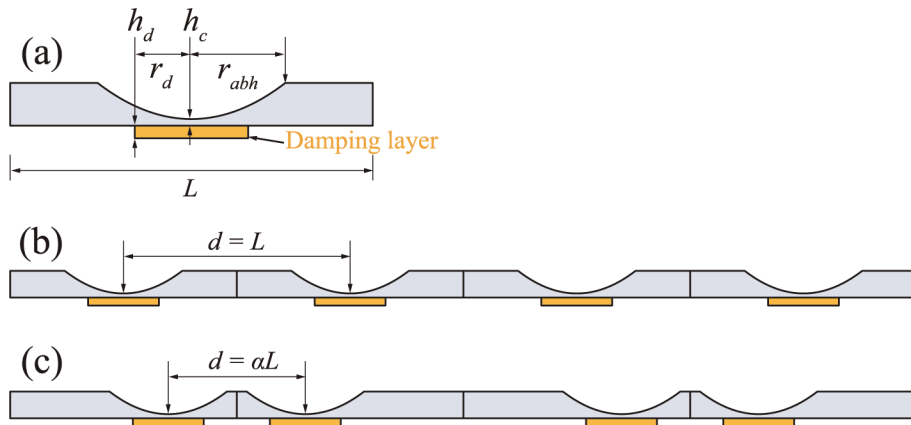


Figure 1. Illustration of (a) a unit ABH cell with detailed geometry parameters, (b) periodic ABHs, and (c) topological ABHs.

2. Wave and Rayleigh-Ritz method

In this section, we will place the focus on the wave and Rayleigh-Ritz (WRRM) to compute the complex dispersion curves. For the ease of exposition, we take the Euler-Bernoulli assumption, such that the bending displacement of the beam can be expanded by a series of basis functions,

$$w(x, t) = \sum_{i=1}^n a_i(t) \varphi_i(x) := \boldsymbol{\varphi}^\top(x) \mathbf{a}(t), \quad (1)$$

where \mathbf{a} is the unknown coefficient vector to be determined and $\boldsymbol{\varphi}$ signifies a Gaussian function vector (see the Gaussian expansion method, GEM [27, 28]).

One can continue in the Rayleigh-Ritz framework to reach the following equation of motion,

$$(\mathbf{K} - \omega^2 \mathbf{M}) \mathbf{A} = \mathbf{0}, \quad (2)$$

where \mathbf{M} and \mathbf{K} respectively denote the mass and stiffness matrices. Please note that in Eq. (2) we have taken $\mathbf{a} = \mathbf{A} \exp(i\omega t)$, where ω represents the angular frequency.

The following step is to impose the Bloch-Floquet periodic conditions at the cell boundaries,

$$w_1 = \lambda w_2, \quad (3)$$

$$\partial_x w_1 = \lambda \partial_x w_2, \quad (4)$$

where w_1 and $\partial_x w_1$ respectively represent the displacement and rotational angle at the left end, and w_2 and $\partial_x w_2$ correspond to the right one. $\lambda = \exp(ikL)$ stands for the propagation constant with k being the wavenumber.

Now inserting Eq. (1) into Eqs. (3) and (4) we have

$$\begin{bmatrix} -\lambda & 0 & 1 & 0 \\ 0 & -\lambda & 0 & 1 \end{bmatrix} \begin{bmatrix} \boldsymbol{\varphi}_2^\top \\ \partial_x \boldsymbol{\varphi}_2^\top \\ \boldsymbol{\varphi}_1^\top \\ \partial_x \boldsymbol{\varphi}_1^\top \end{bmatrix} \mathbf{A} = \begin{bmatrix} 0 \\ 0 \end{bmatrix} =: \tilde{\mathbf{\Lambda}} \boldsymbol{\Phi}^\top \mathbf{A} = \mathbf{0}, \quad (5)$$

where we have identified $\tilde{\mathbf{\Lambda}}$ and $\boldsymbol{\Phi}$.

The key step here is to attain the nullspace basis prescribed by Eq. (5). With the indication in Ref. [29], we can get the basis \mathbf{Z} for $\mathcal{N}(\tilde{\mathbf{\Lambda}} \boldsymbol{\Phi}^\top)$,

$$\mathbf{Z} = [\mathbf{Z}_\varphi, \mathbf{C}_Z] = [\mathbf{Z}_\varphi, \mathbf{C}] \begin{bmatrix} \mathbf{I} & \mathbf{0} \\ \mathbf{0} & \mathbf{Z}_r \end{bmatrix}, \quad (6)$$

where

$$\mathbf{Z}_r := \begin{bmatrix} 1 & 0 \\ 0 & 1 \\ \lambda & 0 \\ 0 & \lambda \end{bmatrix} = \begin{bmatrix} \mathbf{I} \\ \lambda \mathbf{I} \end{bmatrix}, \quad (7)$$

$$\mathbf{Z}_\varphi = \mathcal{N}(\mathbf{\Phi}^\top), \quad (8)$$

and

$$\mathbf{C} = (\mathbf{\Phi}^\top)^+. \quad (9)$$

Assuming the final response \mathbf{A} is linearly constituted by the basis of \mathbf{Z} , that is, $\mathbf{A} = \mathbf{Z}\mathbf{k}$, we arrive at

$$(\mathbf{K} - \omega^2 \mathbf{M})\mathbf{Z}\mathbf{k} = \mathbf{0}, \quad (10)$$

with \mathbf{k} being the unknown vector to be solved. Eq. (10) becomes the equation of motion satisfying the periodic boundary conditions in Eqs. (3) and (4).

To simplify the computation, we define $\mathbf{Z}_c \equiv [\mathbf{Z}_\varphi, \mathbf{C}]$ and

$$\mathbf{Z}_l \equiv \begin{bmatrix} 1 & 0 & \lambda^{-1} & 0 \\ 0 & 1 & 0 & \lambda^{-1} \end{bmatrix} \equiv [\mathbf{I}\lambda^{-1} \quad \mathbf{I}]. \quad (11)$$

Pre-multiplying Eq. (10) by $\text{diag}(\mathbf{I}, \mathbf{Z}_l)\mathbf{Z}_c^\top$ we get

$$\begin{bmatrix} \mathbf{I} & \mathbf{0} \\ \mathbf{0} & \mathbf{Z}_l \end{bmatrix} (\overline{\mathbf{K}} - \omega^2 \overline{\mathbf{M}}) \begin{bmatrix} \mathbf{I} & \mathbf{0} \\ \mathbf{0} & \mathbf{Z}_r \end{bmatrix} \mathbf{k} = \mathbf{0}, \quad (12)$$

where $\overline{\mathbf{K}}_{n \times n} := \mathbf{Z}_c^\top \mathbf{K} \mathbf{Z}_c$ and $\overline{\mathbf{M}}_{n \times n} := \mathbf{Z}_c^\top \mathbf{M} \mathbf{Z}_c$ are square matrices.

Now, it is possible to compute the real dispersion curves once a wavenumber k is given. However, our purpose is to get the complex dispersion curves, where ω is fixed and k is to be determined. To do so, we define $\mathbf{D} \equiv \overline{\mathbf{K}} - \omega^2 \overline{\mathbf{M}}$ and partition it as

$$\mathbf{D}_{n \times n} = \begin{bmatrix} \mathbf{D}_{11, (n-4) \times (n-4)} & \mathbf{D}_{12, (n-4) \times 4} \\ \mathbf{D}_{12, 4 \times (n-4)}^\top & \mathbf{D}_{22, 4 \times 4} \end{bmatrix}. \quad (13)$$

Now, Eq. (12) becomes

$$\begin{aligned} \mathbf{D}_{11} \mathbf{k}_1 + \mathbf{D}_{12} \mathbf{Z}_r \mathbf{k}_2 &= \mathbf{0}, \\ \mathbf{Z}_l \mathbf{D}_{12}^\top \mathbf{k}_1 + \mathbf{Z}_l \mathbf{D}_{22} \mathbf{Z}_r \mathbf{k}_2 &= \mathbf{0}, \end{aligned} \quad (14)$$

where $[\mathbf{k}_1^\top, \mathbf{k}_2^\top] \equiv \mathbf{k}$. Clearing \mathbf{k}_1 we have

$$\mathbf{Z}_l [\mathbf{D}_{22} - \mathbf{D}_{12}^\top \mathbf{D}_{11}^{-1} \mathbf{D}_{12}] \mathbf{Z}_r \mathbf{k}_2 = \mathbf{0}. \quad (15)$$

The Schur complement of \mathbf{D}_{11} can be designated as $\mathbf{G} := \mathbf{D}_{22} - \mathbf{D}_{12}^\top \mathbf{D}_{11}^{-1} \mathbf{D}_{12}$, which can be further partitioned as

$$\mathbf{G} = \begin{bmatrix} \mathbf{G}_{11} & \mathbf{G}_{12} \\ \mathbf{G}_{12}^\top & \mathbf{G}_{22} \end{bmatrix}. \quad (16)$$

Recalling the definition of \mathbf{Z}_l and \mathbf{Z}_r , we can obtain the following equation,

$$\begin{bmatrix} \mathbf{I} & \lambda^{-1}\mathbf{I} \end{bmatrix} \begin{bmatrix} \mathbf{G}_{11} & \mathbf{G}_{12} \\ \mathbf{G}_{12}^\top & \mathbf{G}_{22} \end{bmatrix} \begin{bmatrix} \mathbf{I} \\ \lambda\mathbf{I} \end{bmatrix} \mathbf{k}_2 = (\mathbf{G}_{11} + \mathbf{G}_{22} + \mathbf{G}_{12}^\top \lambda^{-1} + \mathbf{G}_{12} \lambda) \mathbf{k}_2 = \mathbf{0}, \quad (17)$$

which can be converted into a quadratic eigenvalue problem for λ . Therefore, the wavenumber $k \in \mathbb{C}$ can be solved for a given $\omega \in \mathbb{R}$.

3. Numerical results

Once built the computational model, we start to show some numerical results. As shown in **Figure 1**, the lattice constant is selected as $L = 0.1$ m, and the beam thickness at the uniform part is $h_{uni} = 3$ mm. The ABH profile is defined as $h(x) = \varepsilon x^m + h_c$, where $m = 2$, $h_c = 0.6$ mm, $\varepsilon = (h_{uni} - h_c)/r_{abh}^m = 6 \text{ m}^{-1}$, and $r_{abh} = 2$ cm. The beam is made of steel, with Young modulus being $E = 210$ GPa, density $\rho = 7800 \text{ kg/m}^3$, and loss factor $\eta = 0.005$. On the other hand, the damping layer has size $r_d = 2$ cm and $h_d = 1.8$ mm, and the Young modulus $E_d = 5$ GPa, density $\rho_d = 950 \text{ kg/m}^3$, and loss factor $\eta_d = 0.5$.

In the following, we will first examine the complex dispersion curves, then the transmissibilities are inspected to ensure the existence of topological low-frequency bangap.

3.1 Complex dispersion curves

To start with, we do not consider any damping (no damping layer and $\eta = 0$), and a standard periodic cell is considered. As illustrated in **Figure 2a** and **b**, where the real and imaginary parts of the complex dispersion curves have been computed. It is observed that there are two bandgaps appearing in 175–555 Hz and 1635–2330 Hz, respectively. According to the analysis in Ref. [10], those bandgaps are induced by the Bragg scattering effect. Now, we take the supercell (as depicted in **Figure 1b**), with $d = \alpha L$, where $\alpha = 1$. Please note that in this case the bandgaps should occur at the same frequency range. As demonstrated in **Figure 2c** and **d**, this is true, indicating that our WRRM is accurate to recover the complex dispersion curves. Particularly, in **Figure 2d** we found that the evanescent wave is doubled compared to that in **Figure 2b**. This is reasonable because two cells provide more wave attenuation. Please note that there are two passbands and two stopbands in the frequency range of interest (see **Figure 2a**), computed from the periodic cells. However, when using supercell structure, each passband has been divided into two ones (see $f = 50$ Hz and $f = 1040$ Hz), which gives us the possibility to open them in the following content.

Now, we shrink the distance of the ABHs in a supercell (see **Figure 1c**), and set $\alpha = 0.5$. The complex dispersion curves are illustrated in **Figure 3**. It is seen that the passbands are opened at $f = 50$ Hz and $f = 1040$ Hz, and there emerge two new bandgaps in 45–80 Hz and 895–1100 Hz. Since we are more interested in low frequencies, the new first bandgap (45–80 Hz) is much lower than the former one (175–555 Hz). Particularly, we have only changed the ABH distance and the structure has the same weight as before.

At this stage, we include the damping layers and the intrinsic loss of the beam ($\eta = 0.005$). The complex dispersion curves of a supercell with $\alpha = 1$ have been demonstrated in **Figure 4a** and **b**, which are nothing but corresponding to standard periodic lattice. In such a case we see that *bandgaps* no longer exist in the real dispersion curves but in the imaginary part (see **Figure 4b**). Also, in the passbands we also have some wave attenuation because of damping (again see **Figure 4b**).

Once we decrease the ABH distance and set $\alpha = 0.5$ (see **Figure 4c** and **d**), as expected, we can get a new bandgap at very low frequency $f = 95$ Hz. Please note that at very high frequencies the ABH effect starts to take control, so the imaginary part is very smooth and steadily becomes larger over $f = 2000$ Hz.

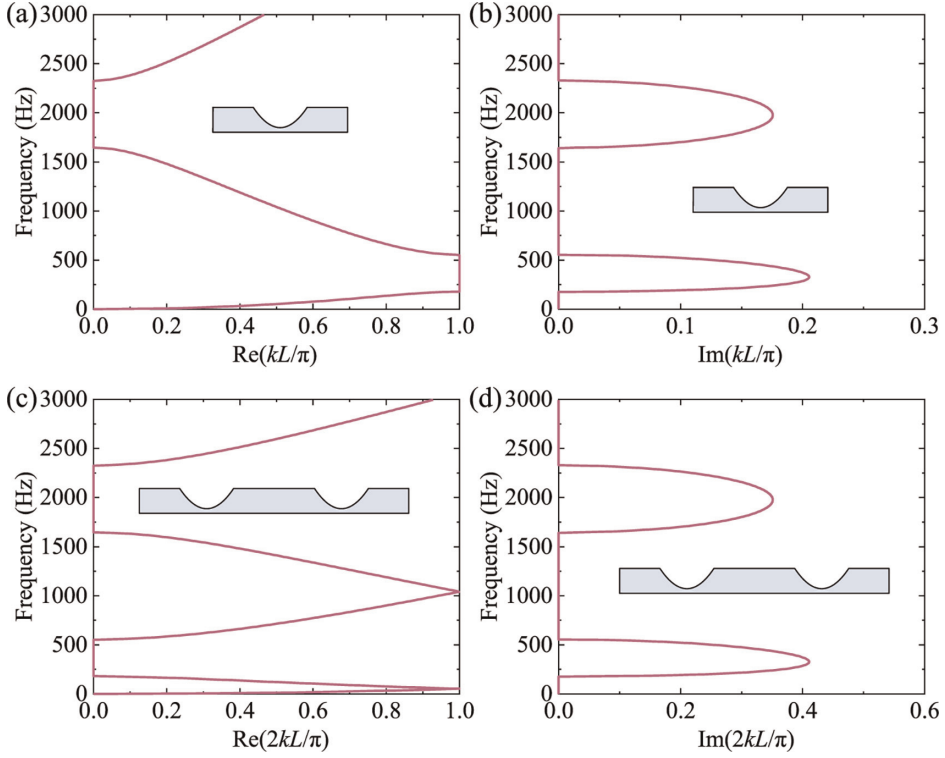


Figure 2. (a) Real and (b) imaginary part of the complex dispersion curves of a standard periodic ABH cell. (c) Real and (d) imaginary part of the complex dispersion curves of a standard periodic supercell. Please note that in this case we have not included the damping layer and beam intrinsic loss.

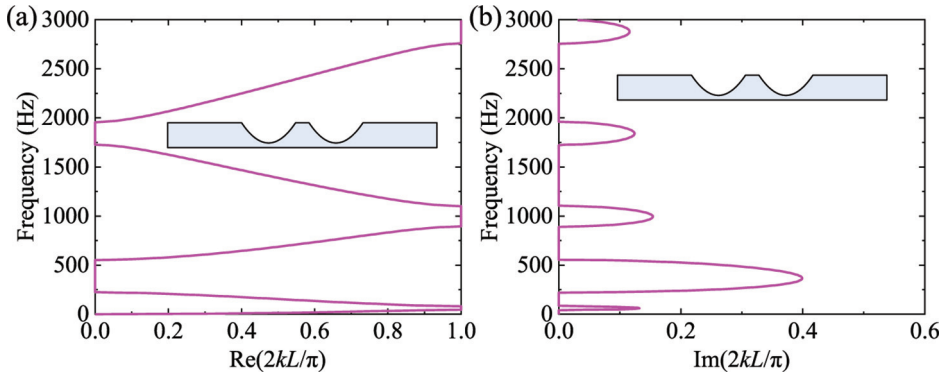


Figure 3. (a) Real and (b) imaginary part of the complex dispersion curves of a topological supercell with $\alpha = 0.5$. Please note that in this case we have not included the damping layer and beam intrinsic loss.

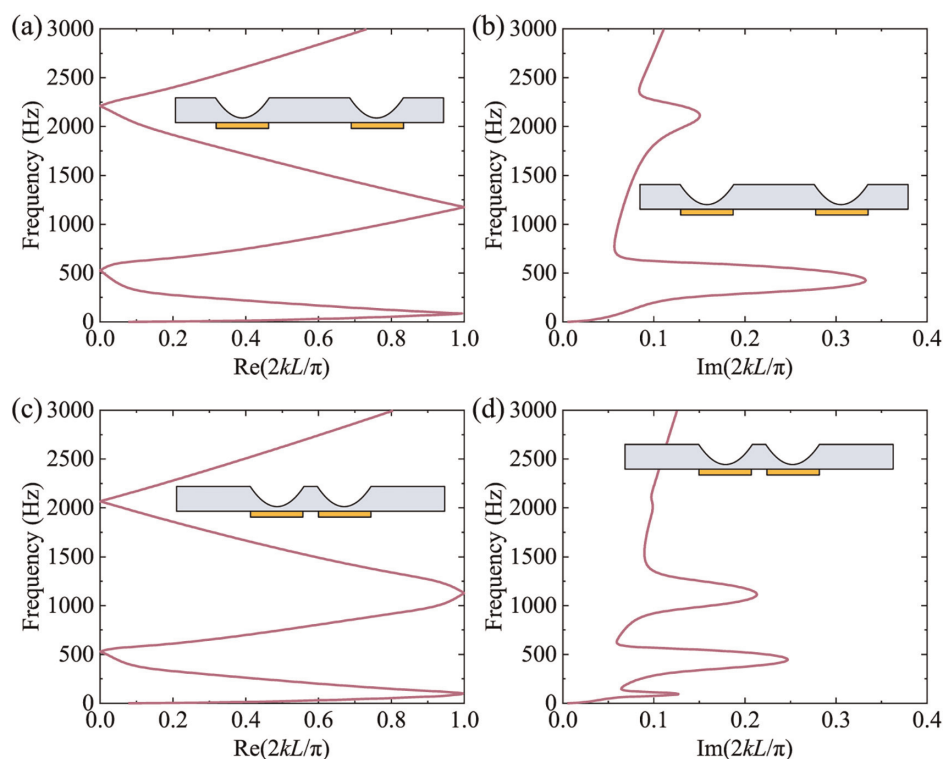


Figure 4. (a) Real and (b) imaginary part of the complex dispersion curves of a standard periodic supercell. (c) Real and (d) imaginary part of the complex dispersion curves of a topological supercell with $\alpha = 0.5$. Please note that in this case we have included the damping layer and beam intrinsic loss.

3.2 Transmissibilities

We next shed light on the wave transmission in finite beams. As usual, we first exclude any damping. In total, 12 cells have been taken into account; thus, the beam

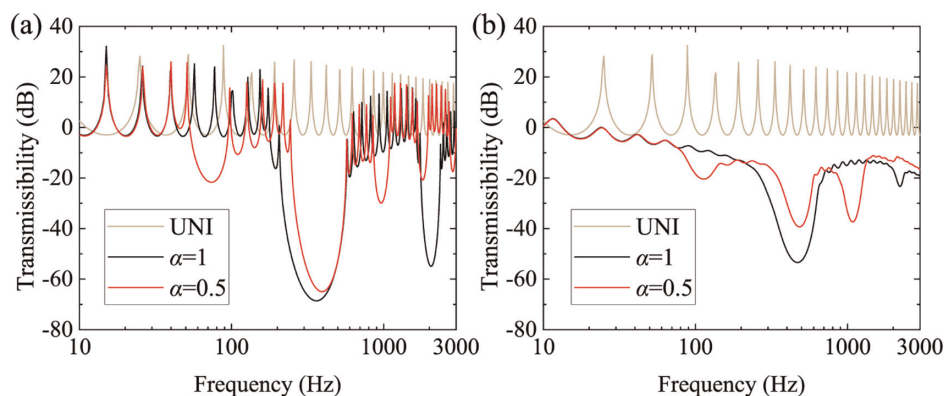


Figure 5. Transmissibilities of finite beams with 12 cells. (a) Without damping layer nor the beam intrinsic loss. (b) With damping layer and the beam intrinsic loss.

length equals to 1.2 m. For reference, we have computed the transmissibility, $T = 10\lg[w^2(1.2)/w^2(0)]$, of a uniform beam (UNI) where a point force is exerted at $x = 0$, see the brown line in **Figure 5a**. For the better inspection of low frequencies, we have chosen logarithmic scale for the frequency axis. Not only that, the T of standard periodic ABH beam has also been computed, see the black line in **Figure 5a**. We can find that two bandgaps take places at the frequency ranges predicted by the dispersion curves in **Figure 2**. Once we have set $\alpha = 0.5$ (see the red curve in **Figure 5a**), we can get a new bandgap centred at 70 Hz.

Once the damping layer and intrinsic loss $\eta = 0.005$ are taken into account, it is seen that vibration peaks are substantially smoothed, especially at high frequencies, where the ABH effect starts working. However, the most intriguing phenomenon is the presence of the low-frequency topological bandgap at $f = 100$ Hz, confirming that the proposed supercell ABH with shrinking distance is very promising for low-frequency vibration reduction.

4. Conclusions

In this chapter, we have proposed a topological ABH metamaterial to generalize a low-frequency bandgap for vibration reduction. Based on a standard periodic ABH beam, we have taken a supercell and reduced the ABH distance, opening new bandgaps, especially at low frequencies.

To characterize such a feature, we have adopted the wave and Rayleigh-Ritz method (WRRM) to compute the complex dispersion curves, which relies on solving the quadratic eigenvalue problem of $k \in \mathbb{C}$ for a fixed $\omega \in \mathbb{R}$. After that, we have analyzed impact of changing the ABH distance on the bandgaps. Before including the damping, the bandgaps can be both appreciated in the real and imaginary parts of the complex dispersion curves. However, after considering the damping, bandgaps can only be inspected in the imaginary part.

Both the analyses on the dispersion curves and transmissibilities indicate that the topological ABHs can indeed produce a low-frequency bandgap, which constitutes a promising low-frequency wave manipulation technique.

Acknowledgements

J. Deng acknowledges the support received by the National Natural Science Foundation of China (52301386) and the support of the Beatriu de Pins postdoctoral program of the Department of Research and Universities of the Generalitat of Catalonia (2022 BP 00027).

Conflict of interest

The author declares no conflict of interest.

Author details


Jie Deng^{1,2}

1 Chongqing Industry Polytechnic College, Chongqing, China

2 Human-Environment Research (HER) Group, Department of Engineering, La Salle, Universitat Ramon Llull C/Quatre Camins, Barcelona, Catalonia, Spain

*Address all correspondence to: dengjie_cn@outlook.com

IntechOpen

© 2024 The Author(s). Licensee IntechOpen. This chapter is distributed under the terms of the Creative Commons Attribution License (<http://creativecommons.org/licenses/by/3.0>), which permits unrestricted use, distribution, and reproduction in any medium, provided the original work is properly cited. 

References

- [1] Huang W, Tao C, Ji H, Qiu J. Enhancement of wave energy dissipation in two-dimensional acoustic black hole by simultaneous optimization of profile and damping layer. *Journal of Sound and Vibration*. 2021;**491**:115764
- [2] Chen X, Jing Y, Zhao J, Deng J, Cao X, Pu H, et al. Tunable shunting periodic acoustic black holes for low-frequency and broadband vibration suppression. *Journal of Sound and Vibration*. 2024;**580**:118384
- [3] Bu Y, Tang Y, Ding Q. Novel vibration self-suppression of periodic pipes conveying fluid based on acoustic black hole effect. *Journal of Sound and Vibration*. 2023;**567**:118077
- [4] Sheng H, He MX, Zhao J, Kam CT, Ding Q, Lee HP. The ABH-based lattice structure for load bearing and vibration suppression. *International Journal of Mechanical Sciences*. 2023;**252**:108378
- [5] Gao W, Qin Z, Chu F. Broadband vibration suppression of rainbow metamaterials with acoustic black hole. *International Journal of Mechanical Sciences*. 2022;**228**:107485
- [6] Zhu H, Semperlotti F. Phononic thin plates with embedded acoustic black holes. *Physical Review B*. 2015;**91**(10): 104304
- [7] Zhu H, Semperlotti F. Anomalous refraction of acoustic guided waves in solids with geometrically tapered metasurfaces. *Physical Review Letters*. 2016;**117**(3):034302
- [8] Zhu H, Semperlotti F. Two-dimensional structure-embedded acoustic lenses based on periodic acoustic black holes. *Journal of Applied Physics*. 2017;**122**(6):065104
- [9] Tang L, Cheng L. Broadband locally resonant band gaps in periodic beam structures with embedded acoustic black holes. *Journal of Applied Physics*. 2017;**121**(19):194901. DOI: 10.1063/1.4983459
- [10] Deng J, Guasch O. On the bandgap mechanism of periodic acoustic black holes. *Journal of Sound and Vibration*. 2024;**579**:118379
- [11] Tang L, Cheng L. Ultrawide band gaps in beams with double-leaf acoustic black hole indentations. *The Journal of the Acoustical Society of America*. 2017;**142**(5):2802-2807
- [12] Zhang Y, Chen K, Zhou S, Wei Z. An ultralight phononic beam with a broad low-frequency band gap using the complex lattice of acoustic black holes. *Applied Physics Express*. 2019;**12**(7): 077002
- [13] Gao N, Guo X, Deng J, Cheng B, Hou H. Elastic wave modulation of double-leaf ABH beam embedded mass oscillator. *Applied Acoustics*. 2021;**173**: 107694
- [14] Park S, Jeon W. Ultra-wide low-frequency band gap in a tapered phononic beam. *Journal of Sound and Vibration*. 2021;**499**:115977
- [15] Tang L, Cheng L, Chen K. Complete sub-wavelength flexural wave band gaps in plates with periodic acoustic black holes. *Journal of Sound and Vibration*. 2021;**502**:116102
- [16] Deng J, Zheng L, Gao N. Broad band gaps for flexural wave manipulation in plates with embedded periodic strip acoustic black holes. *International Journal of Solids and Structures*. 2021;**224**:111043. DOI: 10.1016/j.ijsolstr.2021.111043

- [17] Deng J, Guasch O, Maxit L, Gao N. A metamaterial consisting of an acoustic black hole plate with local resonators for broadband vibration reduction. *Journal of Sound and Vibration*. 2022;**526**:116803
- [18] Deng J, Guasch O, Maxit L, Gao N. Sound radiation and non-negative intensity of a metaplate consisting of an acoustic black hole plus local resonators. *Composite Structures*. 2023;**304**:116423
- [19] Li H, O'donoughue P, Masson F, Pelat A, Gautier F, Touzé C. Broadband shock vibration absorber based on vibro-impacts and acoustic black hole effect. *International Journal of Non-Linear Mechanics*. 2024;**159**:104620
- [20] Deng J, Chen X, Yang Y, Qin Z, Guo W. Periodic additive acoustic black holes to absorb vibrations from plates. *International Journal of Mechanical Sciences*. 2024;**267**:108990
- [21] Deng J, Ma J, Chen X, Yang Y, Gao N, Liu J. Vibration damping by periodic additive acoustic black holes. *Journal of Sound and Vibration*. 2024;**574**:118235
- [22] Deng J, Gao N, Chen X. Ultrawide attenuation bands in gradient metabeams with acoustic black hole pillars. *Thin-Walled Structures*. 2023;**184**:110459
- [23] Wang T, Tang Y, Yang T, Ma ZS, Ding Q. Bistable enhanced passive absorber based on integration of nonlinear energy sink with acoustic black hole beam. *Journal of Sound and Vibration*. 2023;**544**:117409
- [24] Ganti SS, Liu TW, Semperlotti F. Topological edge states in phononic plates with embedded acoustic black holes. *Journal of Sound and Vibration*. 2020;**466**:115060
- [25] Lyu X, Li H, Ma Z, Ding Q, Yang T, Chen L, et al. Numerical and experimental evidence of topological interface state in a periodic acoustic black hole. *Journal of Sound and Vibration*. 2021;**514**:116432
- [26] Deng J, Xu Y, Guasch O, Gao N, Tang L, Chen X. A two-dimensional wave and Rayleigh–Ritz method for complex dispersion in periodic arrays of circular damped acoustic black holes. *Mechanical Systems and Signal Processing*. 2023;**200**:110507
- [27] Deng J, Zheng L, Zeng P, Zuo Y, Guasch O. Passive constrained viscoelastic layers to improve the efficiency of truncated acoustic black holes in beams. *Mechanical Systems and Signal Processing*. 2019;**118**:461–476. DOI: 10.1016/j.ymssp.2018.08.053
- [28] Deng J, Zheng L, Guasch O, Wu H, Zeng P, Zuo Y. Gaussian expansion for the vibration analysis of plates with multiple acoustic black holes indentations. *Mechanical Systems and Signal Processing*. 2019;**131**:317–334. DOI: 10.1016/j.ymssp.2019.05.024
- [29] Deng J, Xu Y, Guasch O, Gao N, Tang L, Guo W. A wave and Rayleigh–Ritz method to compute complex dispersion curves in periodic lossy acoustic black holes. *Journal of Sound and Vibration*. 2023;**546**:117449